



Final Draft **of the original manuscript**

Steppeler, J.; Li, J.; Fang, F.; Navon, M.:

Third-order sparse grid generalized spectral elements on hexagonal cells for uniform-speed advection in a plane.

In: Meteorology and Atmospheric Physics. Vol. 132 (2020) 703 – 719.

First published online by Springer: 23.12.2019

<https://dx.doi.org/10.1007/s00703-019-00718-0>

1 **Third-Order Sparse Grid Generalized Spectral Elements on Hexagonal Cells**
2 **for Uniform-Speed Advection in a Plane**

3 J. Steppeler², J. Li^{1,3*}, F. Fang⁴, I. M. Navon⁵

4
5 ¹International Center for Climate and Environment Sciences, Institute of Atmospheric Physics, Chinese Academy of
6 Sciences, Beijing, 100029, China

7 ²Climate Service Center Germany (GERICS), Fischertwiete 1, Hamburg, 20095, Germany

8 ³Department of Applied Mathematics and Theoretical Physics, University of Cambridge, Wilberforce Road,
9 Cambridge, England CB3 0WA, United Kingdom

10 ⁴Applied Modelling and Computation Group, Department of Earth Science and Engineering, Imperial College
11 London, Prince Consort Road, London, SW7 2AZ, United Kingdom

12 ⁵Department of Scientific Computing, Florida State University, Tallahassee, FL, 32306-4120, United States

13

14 **Corresponding author** J. Li

15 Telephone: +86-10-82995206

16 E-mail: ljx2311@mail.iap.ac.cn

17 ORCID: 0000-0001-8924-5220

18

19

20 **Abstract**

21 This paper investigates sparse grids on a hexagonal cell structure using a Local-Galerkin method (LGM) or generalized
22 spectral element method (SEM). Such methods allow sparse grids to be used, known as serendipity grids in square
23 cells. This means that not all points of the full grid are used. Using a high-order polynomial, some points of each cell
24 are eliminated in the discretization, and thus saving Central Processing Unit (CPU) time. Here a sparse SEM scheme
25 is proposed for hexagonal cells. It uses a representation of fields by second-order polynomials and achieves third-
26 order accuracy. As SEM, LGM is strictly local for explicit time integration. This makes LGM more suitable for
27 multiprocessing computers compared with classical Galerkin methods. The computer time depends on the possible
28 timestep and program implementation. Assuming that these do not change when going to a sparse grid, the potential
29 saving of computer time due to sparseness is 1:2. The projected CPU saving in 3-D from sparseness is by a factor of
30 3:8. A new spectral procedure is used in this paper, called the implied spectral equation (ISE). This procedure allows
31 for some collocation points to use any finite difference scheme of high order and the time derivatives of other spectral
32 coefficients are implied.

33

34 **Keywords**

35 Sparse Grids

36 Spectral Element Methods

37 Hexagonal Grids

38 Local-Galerkin Method

39

40 1. Introduction

41 A new generation of global atmospheric models is constructed by dividing the sphere into patches of nearly
42 regular grids (Taylor et al. 1997; Giraldo 2001; Williamson 2007; Satoh et al. 2008; Skamarock and Klemp 2008;
43 Skamarock et al. 2012; Staniforth and Thuburn 2012; Zängl et al. 2015). The basic principle of such icosahedral or
44 cubed-sphere models has been known for a long time (Williamson 1968; Sadourny 1972). It was about the year 2000
45 until polygonal methods in the form of icosahedral and cubed-sphere models were considered fit for use in realistic
46 atmospheric models (Rancic et al. 1996; Steppeler and Prohl 1996; Ringler et al. 2000). In the mean-time, spectral
47 models or models with latitude-longitude grids became the method of choice for global atmospheric models. At
48 present, most new developments of realistic models use polygonal methods (Taylor et al. 1997; Giraldo 2001;
49 Skamarock and Klemp 2008; Zängl et al. 2015).

50 With hindsight, there are two problems which prevented the immediate application of the polygonal grids
51 (Williamson 1968; Sadourny 1972). One problem is the mapping of the sphere to a plane, which some models employ
52 for the discretization. If a global coordinate is used, this mapping of the sphere to the plane will lead to singularities.
53 This implies similar problems as encountered with global latitude-longitude grids, even though polygonal grids are
54 nearly regular. This problem was solved in Steppeler and Prohl (1996) by abandoning a global coordinate system and
55 rather using a local coordinate at each grid point. In Steppeler et al. (2008), a coordinate-free method was used, which
56 can also be considered as using the earth centered orthogonal coordinate system together with a local basis for vectors
57 at each grid point. Another problem is the occurrence of low-order approximations at poles and edges of the
58 icosahedron. This will lead to the icosahedral grid to be seen distorting the solutions, which is called grid imprinting
59 (Peixoto and Barros 2013; Weller et al. 2012). An example of problems caused by non-uniform approximation order
60 at the poles was given by Tomita et al. (2001). Solutions without grid imprinting were developed in Baumgardner and
61 Frederickson (1985) for second-order approximation and for a non-meteorological problem. In Steppeler et al. (2008),
62 a third-order icosahedral global model without grid imprinting was proposed. Baumgardner and Frederickson (1985)
63 and Steppeler et al. (2008) avoided grid imprinting by using approximations of uniform order two or three. Uniform
64 order p means that there is no grid point where the order of approximation is below p . The grid imprinting reported in
65 Tomita et al. (2001) was caused by approximations going below second-order at poles and icosahedral edges.
66 Baumgardner and Frederickson (1985) obtained successful approximations on the sphere for a non-meteorological
67 problem. Steppeler and Prohl (1996) obtained second-order solutions of the shallow water equations on the sphere

68 and proposed to transfer the approximation principles in Baumgardner and Frederickson (1985). However, the
69 schemes proposed by Baumgardner and Frederickson (1985) and Steppeler et al. (2008) were not mass conserving.

70 To combine high-order approximations on the sphere with mass conservation, finite element method (FEM)
71 or other Local-Galerkin methods (LGMs) can be used (Marras et al. 2016). These methods are naturally conserving
72 and provide a uniform order of approximation. FEMs divide the computational area into cells and use a polynomial
73 representation in each cell to describe the fields. These polynomials can be defined by using several gridpoint values
74 or collocation points for each cell (see Steppeler (1987) for a review). The collocation points are used for the field
75 representation by interpolations in Galerkin methods. The number of collocation points must be sufficient high (e.g.
76 order 2 or order 3) to define a polynomial of the requested order. In this study, we use continuous Galerkin (CG)
77 methods where polynomials fit together continuously at cell boundaries (Taylor et al. 1997; Li et al. 2018).
78 Differentiation of this field representation, to compute the right-hand side of dynamic equations will generally lead
79 out of this continuous function system and create discontinuities at cell boundaries. A Galerkin method is used to map
80 this again to the original function system. Standard time stepping procedures (e.g. Runge-Kutta time integration) can
81 then be applied. The original Galerkin procedure involves the solution of a linear equation system, the mass matrix
82 equation. Even though the mass matrix is often of band diagonal form (Cote et al. 1983), this solution may cause some
83 problems on modern computers. Widely used methods to solve the matrix equation are recursive and the solution may
84 have global impact in one time-step, even though the equation to be solved is local. On massively parallel computers
85 this causes considerable problems, as typically a lot of communication is involved. Approximations to the original
86 Galerkin procedure have been introduced, which make the method local and thus suitable for massively parallel
87 computing. Such approximated or alternative Galerkin procedures are called Local-Galerkin methods. For a general
88 outline of the LGM see Steppeler and Klemp (2017). Discontinuous field representations (DG methods) are used with
89 a variety of LGMs (Cockburn and Shu 2001), but only CG methods are currently near practical use in realistic models.
90 Spectral element methods (SEMs), using Gauss-Lobatto points to define the fields (Giraldo 2001) and the third-degree
91 method (Steppeler, 1976) are examples for LGMs. Considerable progress has been achieved in this way to make high
92 resolution atmospheric modeling possible. CG methods for weather models nearly exclusively use the SEM as LGM
93 (Taylor et al. 1997), being based on the quadrature approximation, since alternative LGMs so far are used with toy
94 models only. In this paper we use a special LGM called Implied Spectral Equations (ISE). With ISE, the definition of
95 some spectral coefficients is implied by the principle of conservation (see details in Section 3).

96 Advantages of SEMs are that they combine an approximation order higher than two with conservation and
97 are of uniform approximation order. The latter means that there exist no grid points such as poles in a global model,
98 where the approximation order drops below a target value. The uniform-order models mentioned above run on the
99 original unsmoothed icosahedral grid on the sphere. SEM models on the sphere, such as Giraldo (2001), combine an
100 approximation order above three with mass conservation. The SEM allows an approximation order higher than two in
101 combination with conservation. Older high-order models, such as that of Kalnay et al. (1977) and Navon and Alperson
102 (1978) were non-conserving. There are alternative possibilities with CG methods to obtain LGMs. Such a method was
103 proposed by Steppeler (1976) which also employed the grid sparsity coming from serendipity elements (Ahlberg et
104 al. 1967). The FEMs with higher than first degree polynomials use sparse grids to represent the fields in each cell.
105 This means that some points of the full grid are omitted in each cell. Such elements with sparse grids are called
106 serendipity elements. They are quite easy to implement with rectangular cells. Their implementation in hexagonal
107 cells is less trivial, but the sparseness factors are larger. The sparse grids can be used in the same way with LGMs as
108 with the original Galerkin procedure (Steppeler 1976).

109 In an ordinary grid system, we call the regular grid the full grid where all the values of fields on the grid
110 points are forecasted. With the sparse grid system, not all grid point values are forecasted, but rather a subset. The
111 non-forecasted points can be computed diagnostically for plotting and other purposes, such as the interface to non-
112 atmospheric models or physical parameterizations. The sparse grids offer a potential saving of computer time. The
113 forecasted grid points in the sparse grid systems form the dynamic grid. These are the points where the dynamic
114 equations are solved. In the following sections, the fields in the hexagonal grid are stored on the full grid, where some
115 points with indices are unused. On computers with many processors this is not optimal, as this may imply message
116 passing for unused points. Therefore, it is desirable to number the points in such a way that no storage is provided for
117 unused points which is called the compact grid representation. Appendix 1 defines a compact grid for hexagonal grids.

118 In this study, we investigate the LGM o2o3 method with hexagonal cells. This method uses second-degree
119 polynomials to represent the field in the cells and the numerical procedure is designed to become third-order by
120 defining the fluxes as piecewise third-order splines. The LGM o3o3 investigated in Steppeler et al (2019) could also
121 have been used and the definition of o3o3 on hexagons is discussed in the appendix. The o3o3 method would have
122 more grid points on each hexagonal cell than o2o3. Therefore, o2o3 is easier to program which is the reason why o2o3
123 was used for the first attempt in this paper. The application of o3o3 in the hexagon is discussed but not tested and

124 implemented in the appendix. We first illustrate the basic hexagonal grid and field representations in Section 2. Section
 125 3 outlines the governing equations and corresponding discrete FDM equations. Section 4 presents a series of idealized
 126 advection test cases with sparse grids. Finally, Section 5 presents a discussion and concludes this study.

127

128 **2. Definition of grids and field representation**

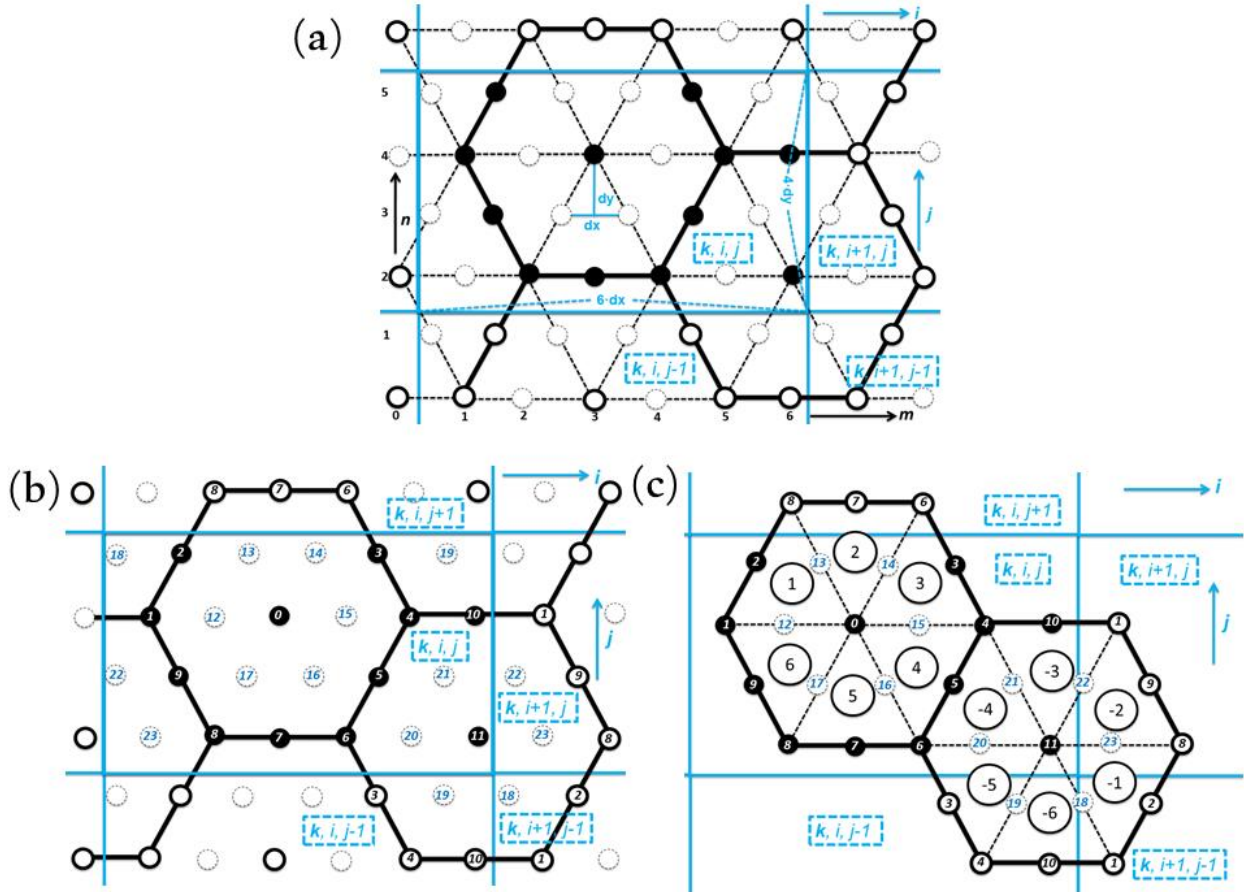
129 Fig. 1a illustrates the grid distribution to cover the computational domain which is divided by the hexagonal
 130 cells. The m, n grid is useful to define a Cartesian grid for the definition of the initial state and plotting. The assignment
 131 of the m, n to the hexagonal points can be seen from Fig. 1a. This is referred to as the Cartesian representation. Let s
 132 be the edge length of the hexagons so that the grid lengths are $dx = \frac{1}{2}s$ and $dy = \frac{\sqrt{3}}{4}s$. The Cartesian coordinates
 133 $x_{m,n}$ and $y_{m,n}$ of the hexagonal points are associated with each point m, n : $m = 0, \dots, M$; $n = 0, \dots, N$.

$$134 \quad x_{m,n} = \begin{cases} mdx & , \text{ for } n \text{ even} \\ mdx + \frac{1}{2}dx, & \text{ for } n \text{ odd} \end{cases} , \quad (1)$$

$$135 \quad y_{m,n} = ndy . \quad (2)$$

136 In the following it is assumed $dx = 1$ and $dy = \frac{\sqrt{3}}{2}$. As seen from Fig. 1a for the full grids there is a one-to-one
 137 correspondence between hexagonal points and the m,n grid. However, though the computational domain can be
 138 separated by the hexagons, the grid points on the edges of the hexagons are shared by two, even three hexagons such
 139 that it is hardly to determine which hexagon the grid belongs to.

140



141
 142 **Fig. 1** The hexagon grid distribution in the computational domain and the index system for the grid point. (a) The
 143 covering of the computational area by hexagonal cells and the non-intersecting elements (k, i, j) indicating that
 144 every grid point is assigned uniquely to one element only: the solid black and white points are dynamic points and
 145 the dashed points are the unused diagnostic points. (b) The index system for every non-intersecting element (k, i, j)
 146 with all dynamic (solid) and diagnostic (dashed) points. (c) The definitions of the grid points in every hexagon with
 147 collocation points and cell-related indices: the indices $-6, -5, \dots, -1, 1, 2, \dots, 6$ in the circles with bigger size are used
 148 for numbering the six triangles in each hexagon.

149
 150 In order to assign every grid point to only one computational element, we introduce a new index system
 151 and the corresponding non-intersecting element (k, i, j) (the blue rectangles in Fig. 1) where the structured indices
 152 are $i = 0, \dots, i_e, j = 0, \dots, j_e$ and $k = (0, \dots, k_e)$ is the index pointing to a particular point. If $k_e = 23$, then the grid is

153 regarded as the full grid system, including all the points numbering from 0 to 23 in one blue rectangular in Fig. 1b. If
 154 $k_e = 11$, then the grid is regarded as the sparse grid system, including all black points numbering from 0 to 11 in one
 155 blue rectangular in Fig. 1b. For the sparse grid, the points numbering from 12 to 23 are unused diagnostic. Therefore,
 156 the grid points within non-intersecting element (k, i, j) are designed for achieving the one-to-one correspondence
 157 and coding. The transformation between the indices (k, i, j) and m, n is seen from Figs. 1a and 1b. Comparing the
 158 new index system (k, i, j) (the light blue index) and the m, n grid system (the black index) in Fig. 1a, every non-
 159 intersecting element contains six m -points in the horizontal while four n -points in the vertical.

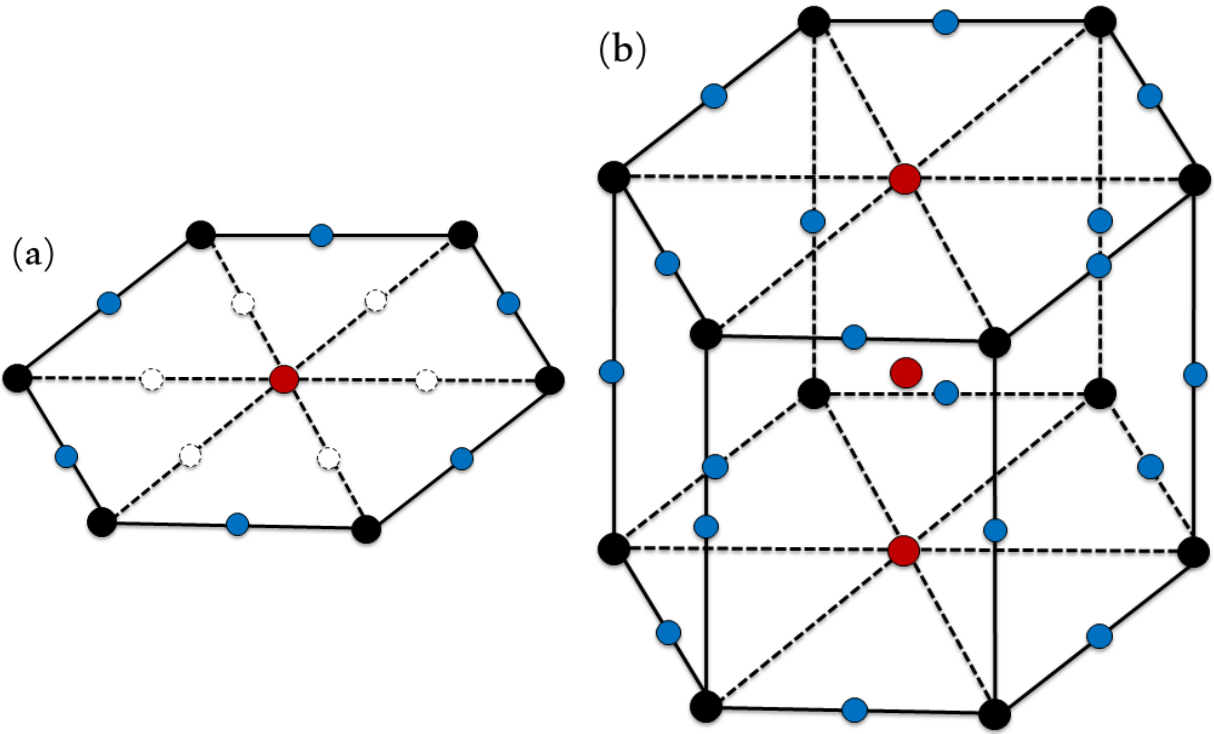
160 To define a numerical scheme, it is necessary to have unique indices for each point which is shown in Fig.
 161 1b for the computer implementation. This can be naturally done using an unstructured gridding. Alternatively, any 3-
 162 D model using unstructured indexing can be adapted to the hexagonal scheme. In this study, we use a sparse structured
 163 programming indexed by (k, i, j) in 2-D. Therefore, the compact grid defines the sparse grid ($k_e = 11$) without
 164 assigning memory storage to unused points which implies that a 3-D realization could be done using any structured
 165 3-D model as a basis. When using the Cartesian grid for the representation of the sparse grid, though half of the points
 166 m, n are unused, these grids still occupy a considerable proportion of the storage and message capacity with
 167 multiprocessing. It is a waste of computational resources and only acceptable for research models.

168 To achieve a numerical scheme, it is important to design the field representation. In every element (k, i, j)
 169 , there are two centers ($k = 0$ and 11) of the hexagons such that we discuss the field representations in two different,
 170 but similar hexagons with center points numbering $k = 0$ and 11 shown in Fig. 1c. In each hexagon, there are 19 points
 171 for potential use to define amplitudes for the field representation by second-degree polynomials. Solid points with
 172 indices $k = 1, 4, 6, 8$ in element (k, i, j) , $k = 6, 8$ in element $(k, i, j + 1)$, $k = 1, 8$ in element $(k, i + 1, j)$, $k = 1$ in
 173 element $(k, i + 1, j - 1)$ and $k = 4$ in element $(k, i, j - 1)$ are the corner points and points with indices $k = 2, 3, 5, 7,$
 174 $9, 10$ in element (k, i, j) , $k = 7$ in element $(k, i, j + 1)$, $k = 9$ in element $(k, i + 1, j)$, $k = 2$ in element
 175 $(k, i + 1, j - 1)$ and $k = 3, 10$ in element $(k, i, j - 1)$ are the edge points on the boundaries. Points with indices $k =$
 176 $12, 13, 14, 15, 16, 17, 20, 21$ in element (k, i, j) , $k = 18$ in element $(k, i + 1, j - 1)$, $k = 22, 23$ in element

177 $(k, i+1, j)$ and $k = 19$ in element $(k, i, j-1)$ is the interior points which can be used for the second-order full grid
178 systems, not for sparse grid. Except for the center point $k = 0, 11$ in element (k, i, j) , all dynamic points are located
179 on cell boundaries. In order to obtain the field representation by polynomials, interior points will be defined
180 diagnostically using dynamic amplitudes.

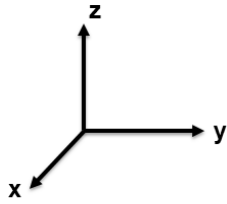
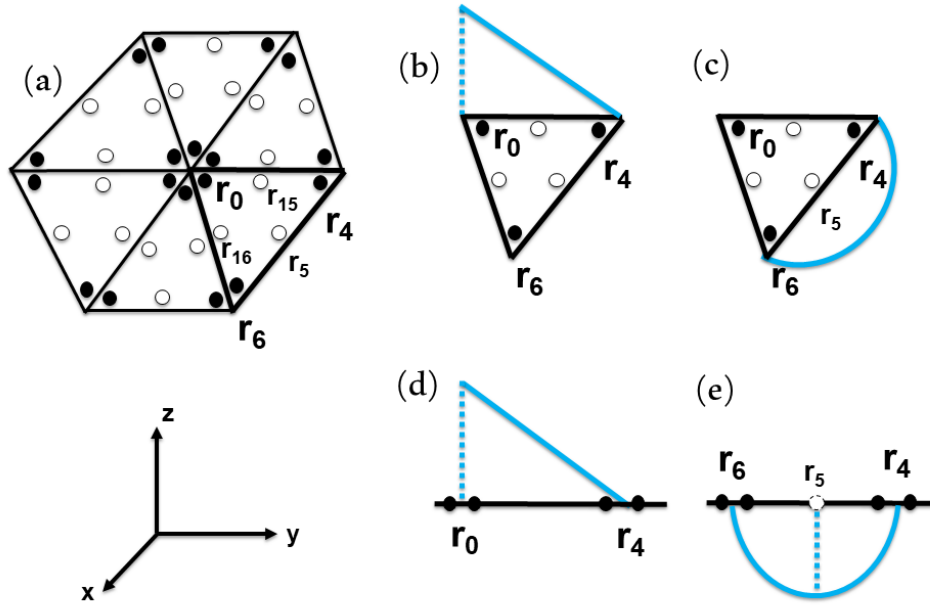
181 Since the corner and edge points on boundaries of hexagons belong to more than one hexagon, the weights
182 of center, edge, corner and interior points shared in each hexagon are $1, \frac{1}{2}, \frac{1}{3}, 1$ in 2-D hexagonal grid such that the
183 number of independent amplitudes in each hexagon is $1 \times 1 + \frac{1}{2} \times 6 + \frac{1}{3} \times 6 + 1 \times 6 = 12$ (Fig. 2a). In this study, as a
184 sparse grid is used, we will not use the dashed interior points as dynamic points. These points are shown in Fig. 2a
185 and not shown in Fig. 2b. Dynamic points for this sparse grid system are solid points. When going to a sparse grid
186 system, the potential saving of computer time due to sparseness is 1:2 in 2-D (Fig. 2a) under the assumption of the
187 same timestep and the CPU time per dynamic point for both cases. In 3-D hexagonal box (Fig. 2b), there are two
188 layers (the bottom and middle layers) containing different numbers of dynamic point. The bottom layer contains six
189 corner, one center and six horizontal edge points with the weights of $\frac{1}{3}, 1, \frac{1}{2}$, while the middle layer contains six
190 vertical edges, each shared by three boxes and the center point. Therefore, the middle layer contains $\frac{1}{3} \times 6 + 1 = 3$
191 dynamic points and the full grid points are for the middle layer the same as for the bottom layer which means the 3-D
192 sparseness factor is 9:24 (3:8).

193



194
 195 **Fig. 2** 2-D (a) and 3-D (b) hexagonal grid box where the red, black and blue points are center, corner and edge
 196 points. The white dashed points in (a) are the interior (unused) points which do not show in (b).

197
 198 In this study, basis functions used for the field representation can be first- and second-order in each triangle
 199 respectively. In the following, we set one triangle in the element (k, i, j) as an example with numbered corners
 200 $\mathbf{r}_{0,i,j}, \mathbf{r}_{4,i,j}, \mathbf{r}_{6,i,j}$. The distribution of triangles and corner and edge points between the hexagonal cells can be seen in
 201 Fig. 3. Note that the amplitude of the field for each point belongs to more than one triangle and one hexagon: each
 202 corner amplitude belongs to one hexagonal cell if it locates at a center point $\mathbf{r}_{0,i,j}$ and to three hexagonal cells if it
 203 locates at hexagonal corner point $\mathbf{r}_{4,i,j}, \mathbf{r}_{6,i,j}$. An edge amplitude belongs to two hexagons and two triangles when it
 204 locates at edge points $\mathbf{r}_{5,i,j}$. As seen from Fig. 3, there exist edge points $\mathbf{r}_{15,i,j}, \mathbf{r}_{16,i,j}$ for two triangles, which are
 205 interior points of a hexagon, meaning that they are triangular edge points, but not hexagonal edge points. From Fig.
 206 3, these relations become clear.



208

209 **Fig. 3** The first-order and second-order basis functions defined in one triangle within a hexagon centered at point

210

$\mathbf{r}_{0,i,j}$ for field representation.

211

212 The triangular amplitudes are defined at corners: $\mathbf{r}_{0,i,j}, \mathbf{r}_{4,i,j}, \mathbf{r}_{6,i,j}$ and edges $\mathbf{r}_{5,i,j}, \mathbf{r}_{15,i,j}, \mathbf{r}_{16,i,j}$, where

213 $\mathbf{r}_{5,i,j} = \frac{1}{2}(\mathbf{r}_{4,i,j} + \mathbf{r}_{6,i,j}), \mathbf{r}_{15,i,j} = \frac{1}{2}(\mathbf{r}_{0,i,j} + \mathbf{r}_{4,i,j}), \mathbf{r}_{16,i,j} = \frac{1}{2}(\mathbf{r}_{0,i,j} + \mathbf{r}_{6,i,j})$. The corner points determine the linear

214 basis functions $e(\mathbf{r})$ (Figs. 3b and 3d). We provide the basis functions for the case of irregular triangles, even though

215 we use only the regular case in this paper. Without loss of generality, we give the basis function belonging to corner

216 point $\mathbf{r}_{0,i,j}$ and edge point $\mathbf{r}_{0,i,j}^\perp$ defined at $\mathbf{r}_{0,i,j}^\perp = \frac{1}{2}(\mathbf{r}_{4,i,j} + \mathbf{r}_{6,i,j})$. The unit vector of the mid-line combining

217 corner point $\mathbf{r}_{0,i,j}$ and edge point $\mathbf{r}_{0,i,j}^\perp$ is defined as $\mathbf{n}_{0,i,j}^m = \frac{\mathbf{r}_{0,i,j}^\perp - \mathbf{r}_{0,i,j}}{|\mathbf{r}_{0,i,j}^\perp - \mathbf{r}_{0,i,j}|}$ and the unit perpendicular vector is

218 defined as $\mathbf{n}_{0,i,j}^s = \frac{\mathbf{r}_{6,i,j} - \mathbf{r}_{4,i,j}}{|\mathbf{r}_{6,i,j} - \mathbf{r}_{4,i,j}|}$. We introduce the local coordinates (λ, μ) for each triangular corner as a non-

219 orthogonal coordinate:

220
$$\mathbf{r} = \lambda \mathbf{n}_{0,i,j}^m + \mu \mathbf{m}_{0,i,j}^s \quad (3)$$

221 and define the linear corner basis function e_0 at corner point $\mathbf{r}_{0,i,j}$ as

222
$$e_0(\mathbf{r}) = e_0(\lambda, \mu) = 1 - \frac{2}{\sqrt{3}} \lambda \quad (4)$$

223 Therefore, each corner point defines a linear basis function $e(\mathbf{r})$ inside the triangle while outside the triangle, these
 224 linear basis functions are defined to be zero. This linear basis function, belonging to corner point $\mathbf{r}_{0,i,j}$ is the linear
 225 function being 1 at $\mathbf{r}_{0,i,j}$ and 0 at $\mathbf{r}_{4,i,j}, \mathbf{r}_{6,i,j}$.

226 Three second-order basis functions are associated with the edge points $\mathbf{r}_{5,i,j}, \mathbf{r}_{15,i,j}, \mathbf{r}_{16,i,j}$ in the triangle.
 227 Without loss of generality, we assume that the center of coordinates is at $\mathbf{r}_{0,i,j}$, meaning $\mathbf{r}_{0,i,j} = 0$, for the definition
 228 of this basis function. We define one of the second-order basis functions as $b_{p,g}^2(\mathbf{r})$, which is associated with the
 229 edge point $\mathbf{r}_{4,6,i,j} = \frac{1}{2}(\mathbf{r}_{4,i,j} + \mathbf{r}_{6,i,j}) = \mathbf{r}_{5,i,j}$ (Figs. 3c and 3e). Then we define $\mathbf{r}_{4,i,j}^\perp$ and $\mathbf{r}_{6,i,j}^\perp$ to be a set of vectors
 230 orthogonal to $\mathbf{r}_{4,i,j}$ and $\mathbf{r}_{6,i,j}$. Therefore, the second-order basis function in this triangle is set as:

231
$$b_{p,g}^2(\mathbf{r}) = \frac{b_{p,g}'^2(\mathbf{r})}{(\mathbf{r}_{4,i,j}^\perp \cdot \mathbf{r})(\mathbf{r}_{6,i,j}^\perp \cdot \mathbf{r})}, \quad (5)$$

232 where $b_{p,g}'^2(\mathbf{r}) = \begin{cases} (\mathbf{r}_{4,i,j}^\perp \cdot \mathbf{r})(\mathbf{r}_{6,i,j}^\perp \cdot \mathbf{r}), & \Delta \text{ with corner points 4,6 in hexagon centered at point 0} \\ 0, & \text{outside } \Delta \text{ with corner points 4,6} \end{cases}$, the dot between two vectors

233 indicates the dot product and $b_{p,g}^2(\mathbf{r}_{4,6,i,j}) = b_{p,g}^2(\mathbf{r}_{5,i,j}) = 1$. Note that all basis functions defined above are
 234 discontinuous. If, however, all basis functions belonging to the same corner or edge point are summed, the result will
 235 be a continuous basis function. From this follows, that using all corner and edge amplitudes and summing over all
 236 basis functions will result in a continuous field.

237 Now let the field $h(\mathbf{r})$ be given at all corner and edge points of the hexagonal grids. We give the
 238 representation formula for triangular amplitudes. For a hexagonal grid, let the corner point amplitudes be $\mathbf{r}_{p,i,j}$ and

239 the edge amplitudes be $\mathbf{r}_{p,q,i,j}$. Note that edge points and edge amplitudes are defined only if $\mathbf{r}_{p,i,j}$ and $\mathbf{r}_{q,i,j}$ are
 240 immediate neighbours. Then we have the general form of the field representation for $h(\mathbf{r})$ in the hexagonal grid
 241 with center point 0:

$$242 \quad h(\mathbf{r}) = \sum_{\text{six } \Delta\text{s in one hexagon}} \left[\sum_p h_p e_p(\mathbf{r}) + \sum_{p,q \text{ are neighbours}} h_{p,q} b_{p,q}^2(\mathbf{r}) \right], \quad (6)$$

243 where h_p is the corner amplitude and $h_{p,q}$ is the edge amplitude. Eq. (6) means that the field is determined by
 244 corner amplitudes h_p and edge amplitudes $h_{p,q}$, where the corner and edge amplitudes are all dynamic points and
 245 the six interior amplitudes are determined by the surrounding amplitudes on the boundaries and the center of the
 246 hexagon. Alternatively, there is another intuitive representation of the field $h(\mathbf{r})$ which is defined as:

$$247 \quad h(\mathbf{r}) = \sum_{\text{six } \Delta\text{s in one hexagon}} \left[\sum_{p=0}^9 h_p e_{(p,i,j),\Delta}^c(\mathbf{r}) + \sum_{p=12}^{17} h_p e_{(p,i,j),\Delta}^c(\mathbf{r}) + \sum_{p=6}^8 h_p e_{(p,i,j+1),\Delta}^c(\mathbf{r}) \right], \quad (7)$$

248 where $e_{(p,i,j),\Delta}^c(\mathbf{r}) = \begin{cases} 1, & \mathbf{r} \in \Delta \text{ \& } [(p,i,j),\Delta] \text{ see in Tab. 1} \\ 0, & \text{else} \end{cases}$ are the characteristic basis functions for each

249 point and each triangle in the hexagonal grid with center point 0 (see (p, Δ) in Tab. 1). This is hardly used for program
 250 implement while is convenient and intuitive to understand how to represent the field. Once the triangles and grid
 251 points in one hexagon meet the conditions of the combination in Tab. 1, the value of the basis function $e_{(p,i,j),\Delta}^c(\mathbf{r})$
 252 can be determined.

253
 254 **Table 1** List of triangle numbers Δ belonging to a grid point p meaning that basis function $e_{(p,i,j),\Delta}^c(\mathbf{r})$ is equal to
 255 one being different from zero.

Point	Triangle number Δ	Point p	Triangle number Δ	Point p	Triangle number Δ
p					

$0,i,j$	$(0,i,j),1 \& (0,i,j),2 \& (0,i,j),3 \& (0,i,j),4 \& (0,i,j),5 \& (0,i,j),6$	$1,i,j$	$(1,i,j),1 \& (1,i,j),6$	$2,i,j$	$(2,i,j),1$
$3,i,j$	$(3,i,j),3$	$4,i,j$	$(4,i,j),3 \& (4,i,j),4$	$5,i,j$	$(5,i,j),4$
$6,i,j$	$(6,i,j),4 \& (6,i,j),5$	$7,i,j$	$(7,i,j),5$	$8,i,j$	$(8,i,j),5 \& (8,i,j),6$
$9,i,j$	$(9,i,j),6$	$12,i,j$	$(12,i,j),1 \& (12,i,j),6$	$13,i,j$	$(13,i,j),1 \& (13,i,j),2$
$14,i,j$	$(14,i,j),2 \& (14,i,j),3$	$15,i,j$	$(15,i,j),3 \& (15,i,j),4$	$16,i,j$	$(16,i,j),4 \& (16,i,j),5$
$17,i,j$	$(17,i,j),5 \& (17,i,j),6$	$6,i,j+1$	$(6,i,j+1),2 \& (6,i,j+1),3$	$7,i,j+1$	$(7,i,j+1),2$
$8,i,j+1$	$(8,i,j+1),1 \& (8,i,j+1),2$				

256

257

258

259

260

261

262

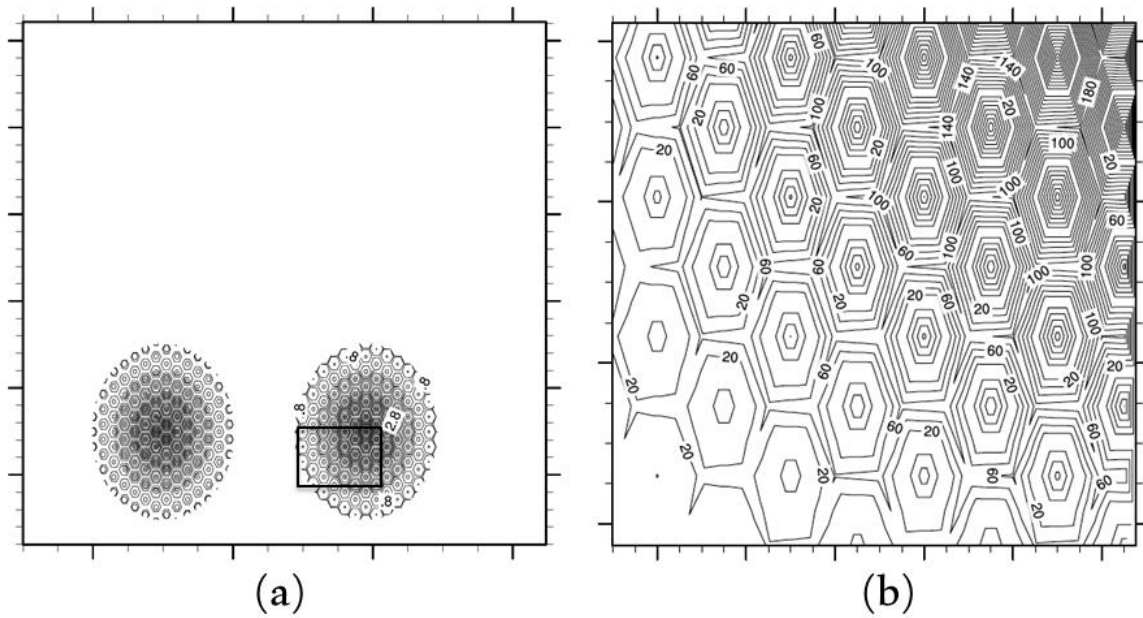
263

264

265

266

Note that the amplitudes of interior hexagonal edge points are diagnostic which means that the interior points in the hexagon are unused in the sparse grid scheme. However, unused points can be interpolated to achieve a full grid, which can be used for plotting, if one does not want to go for this purpose to the Cartesian representation. The interpolation of unused points from dynamic points results in smooth plots of fields. If the unused points are filled with the value of zero, the grid structure can be seen in Fig. 4 which shows a plot of a part of the field on the used points, when the field is defined zero on the unused points. The hexagonal structure becomes visible, with the corners, edges and centers showing local maxima, providing a good indication of the hexagonal cell boundaries. According to Fig. 4, the small hexagons inside the large ones are those where the points are unused for dynamics and put to values of zero.



267

268 **Fig. 4** A schematics of the field using unconventional plotting. (a) The field and the field shifted to the right
 269 (only the used points are shifted to the right). The amplitudes at the unused points remain at their original position.
 270 This way of plotting shows fields which add up to a smooth function, if the right part of (a) is shifted to the left again.
 271 The right and left parts of (a) are like the positive and negative of a picture. (b) shows the details of a part of the field
 272 in (a) marked with a black rectangle. As the amplitude of unused points is set to zero, the hexagonal grid structure
 273 becomes visible.

274

275 3. The construction of finite difference formula

276 The principle of Galerkin method is to represent fields piecewise as polynomials. By using a number of
 277 collocation grid points within each element, the discretization on hexagonal cells can be written as a FDM
 278 scheme based on the structured index (i, j) as indicated in Fig. 1. For the sparse grid scheme, only half of points (the
 279 solid black grid points shown in Fig. 1c) are used, which demonstrates that a compact data structure is possible which
 280 may turn to be handy for realistic applications. Different from the ordinary FDM schemes where the same form of
 281 schemes is used in different elements, these schemes use different FDM equations for the collocation points indexed

282 by k in each element (k, i, j) and the formula for the different k have to be programmed each differently. However,
 283 for the same k and different (i, j) in Fig. 1c, the FDM schemes are analogous.

284 In the present paper, a new LGM, implied spectral equation (ISE), is used in which mass conservation in a
 285 center point is used to define the corresponding spectral amplitudes, while other amplitudes on the edge and corner
 286 points are provided by any high-order FDM scheme with the target order. If all amplitudes of all points in a hexagon
 287 except the center point are computed, the balance equation for the amplitude at the center point can be written as an
 288 equation for the time derivative of the center amplitude. This is analogous to the procedure used with the o3o3 scheme
 289 (Steppeler et al. 2019). This mass balancing ISE method, known from SEM described by Steppeler (1987) for a large
 290 range of LGMs will be used to achieve mass conservation when using the quadrature approximation. This means for
 291 our method of hexagons that mass conservation needs to be a consideration only for the center point whilst other
 292 points can be treated by differentiating along straight lines. It will be shown in the following that how the principle of
 293 mass conservation allows to compute the time derivative of the spectral amplitudes at center point which is then
 294 transformed to gridpoint space to obtain a conserving scheme. The FDM schemes used may not refer to the spectral
 295 representation and will normally use points on a straight line for efficiency. A minimum of one implied spectral
 296 amplitude is sufficient to obtain an overall mass-conserving scheme.

297 In details, we use the advection equation

$$298 \quad \partial_t h = -u \cdot \partial_x h - v \cdot \partial_y h, \quad (8)$$

299 as a test where u, v are assumed to be constant and $\partial_t h, \partial_x h, \partial_y h$ indicates the differentiation of variable h with
 300 respective to t (time), x and y (location).

301 Most derivatives used to compute the divergence are obtained by differencing along lines and taking
 302 directional derivatives. Let $\mathbf{n}_l = (n_l^x, n_l^y)$ be any unit vector along a line l . The l -directional derivative of a function
 303 $h(\mathbf{r} + l \cdot \mathbf{n}_l)$ is defined as:

$$304 \quad \partial_l h(\mathbf{r} + l \cdot \mathbf{n}_l) = n_l^x \partial_x h(r^x + l \cdot n_l^x, r^y + l \cdot n_l^y) + n_l^y \partial_y h(r^x + l \cdot n_l^x, r^y + l \cdot n_l^y), \quad (9)$$

305 where $\mathbf{r} = (r^x, r^y)$ is the position vector of the corresponding point and l is the differential length along the unit
 306 vector \mathbf{n}_l direction. In the following, it is assumed that $l = 1$, without loss of generality and take $\mathbf{n}_l = (1, 0)$ and $u = 1$
 307 as an example. Therefore, Eq. (8) becomes

$$308 \quad \partial_l h = -u \cdot \partial_x h = -\partial_x h, \quad (10)$$

309 where the advection is homogeneous with a constant velocity field. Note that if we have calculated the FDM formula
 310 for $\partial_x h$, we can obtain the FDM formula for $\partial_l h$ and vice versa. For our simple example the time derivative is the
 311 space derivative.

312 According to Fig. 1c, the first-order directional derivatives at edge points 2, 3, 5, 7, 9, 10 will be called

313 $\partial_l h = -\partial_l h(\mathbf{r}_{k,i,j}) = -\delta_x h(\mathbf{r}_{k,i,j})$ and for example $k = 7$ in Fig. 1c is computed by:

$$314 \quad \delta_x h(\mathbf{r}_{7,i,j}) = h(\mathbf{r}_{6,i,j}) - h(\mathbf{r}_{8,i,j}), \quad (11)$$

315 which is given to compute flux divergences or derivatives in x - and y -directions in edge points.

316 The second-order derivative $\delta_x^2 h_{7,i',j'}$ at point $k = 7$ in Fig. 1c is computed by:

$$317 \quad \delta_x^2 h(\mathbf{r}_{7,i,j}) = -8 \left\{ h(\mathbf{r}_{7,i,j}) - \frac{1}{2} [h(\mathbf{r}_{6,i,j}) + h(\mathbf{r}_{8,i,j})] \right\}. \quad (12)$$

318 For the third-order derivative at the same point we define:

$$319 \quad \delta_x^3 h(\mathbf{r}_{7,i,j}) = -\frac{7}{16} [h(\mathbf{r}_{6,i,j}) - h(\mathbf{r}_{8,i,j})] - \frac{1}{48} [h(\mathbf{r}_{11,i,j}) - h(\mathbf{r}_{11,i-1,j})]. \quad (13)$$

320 For the other edge points, the formula is analogous.

321 A third-order accurate formula for the directional derivative along the line l between the points 8 and 6 in
 322 Fig. 1c is:

$$323 \quad \partial_l h = \delta_x h(\mathbf{r}_{7,i,j}) + \delta_x^2 h(\mathbf{r}_{7,i,j}) w_{i,j}^2(\mathbf{r}_{7,i,j}) + \delta_x^3 h(\mathbf{r}_{7,i,j}) w_{i,j}^3(\mathbf{r}_{7,i,j}). \quad (14)$$

324 where $w_{i,j}^2$ and $w_{i,j}^3$ are the weight coefficients and $\delta_x^2 h(\mathbf{r}_{7,i,j}) w_{i,j}^2(\mathbf{r}_{7,i,j}) = 0$.

325 The derivations Eqs. (11)-(14) use the relations between third-, second- or first-order derivatives along
 326 straight lines combining points 8 and 6. Coordinate lines can be arbitrarily tilted to each other, but for the success of
 327 this method, it is necessary that some pieces of the lines are not curved, so that numerical differentiation along the

328 lines is possible. The equations may appear rather difficult (see a considerable simplification and details in Appendix
 329 1). The third-order derivative is obtained from point 7 in Fig. 1c and four more points being on a straight line. For
 330 practical modelers, it may be easier to differentiate in third-order approximation along this line, for which five points
 331 are sufficient. Unfortunately, the points are irregular, as the two points out of the hexagon have three times the distance
 332 from the center point $k = 7$ as the two interior points $k = 6$ and 8. Therefore, if weights for irregular differentiation are
 333 obtained numerically, the rather complicated derivations above could be replaced by simple finite differences on
 334 irregular grids on lines which are not necessarily in x - or y -directions. For example, the high-order derivative computed
 335 in Eq. (11) is obtained by

$$336 \quad \partial_x h(\mathbf{r}_{7,i,j}) = w_1 h(\mathbf{r}_{11,i,j}) + w_2 h(\mathbf{r}_{6,i,j}) + w_3 h(\mathbf{r}_{7,i,j}) + w_4 h(\mathbf{r}_{8,i,j}) + w_5 h(\mathbf{r}_{11,i-1,j}), \quad (15)$$

337 whose indices are taken from Fig. 1c. The weights w_1, w_2, w_3, w_4, w_5 are obtained numerically for $l = 1$ as
 338 $w_1 = -\frac{1}{48}, w_2 = \frac{9}{16}, w_3 = -0.0, w_4 = -\frac{9}{16}, w_5 = \frac{1}{48}$. The numerical procedure can also handle the more irregular
 339 case, which would appear for discretizations on the sphere. It is in principle possible to compute fluxes in x - or y -
 340 directions by using just two directional derivatives (see below). This was done by Steppeler et al. (2008) where the
 341 stability was achieved because the directional derivatives were taken as centered differences.

342 Here we have three directional derivatives available at corner points 1, 4, 6, 8. At corner points, as the
 343 derivatives are one-sided, an average of all three directional derivatives will be needed generally to have the chance
 344 of a stable scheme. To have a guide for the averaging of derivatives at corner points, infinitesimal control volumes are
 345 used. Fig. 5 shows a FDM stencil at a corner point. It could be identical to the stencil with target point 4 in Fig. 1c. A
 346 heuristic consideration is done to obtain reasonable weights for averaging the derivative at the target point 4. We
 347 define the directional vectors as $\mathbf{n}_{k,tg} = \mathbf{r}_k - \mathbf{r}_{tg}$ (here, k denotes one of three points linked to the target point $tg=4,i,j$,
 348 see Fig. 5) and the corresponding directional derivative $\partial_{\mathbf{n}_{k,tg}} h_{tg}$ at the target point tg . We can obtain three directional
 349 vectors $\mathbf{n}_{1,i+1,j;4,i,j} = \mathbf{r}_{1,i+1,j} - \mathbf{r}_{4,i,j}$, $\mathbf{n}_{6,i,j;4,i,j} = \mathbf{r}_{6,i,j} - \mathbf{r}_{4,i,j}$, $\mathbf{n}_{6,i,j+1;4,i,j} = \mathbf{r}_{6,i,j+1} - \mathbf{r}_{4,i,j}$ observing in Fig. 5.
 350 Here we describe the x -direction advection equation. The y -direction is treated in an analogous way. Then, we obtain
 351 the integral of the flux $fl(\mathbf{r}_{4,i,j})$ through the surface in Fig. 5:

352
$$\oint_{\Omega_4} fl(\mathbf{r}_{4,i,j}) \mathbf{n} \cdot d\mathbf{s} = \sum_{(k,i',j')=(6,i,j+1),(6,i,j),(1,i+1,j)} \left[\partial_{\mathbf{n}_{k,i',j';4,i,j}} h(\mathbf{r}_{4,i,j}) \cdot \left(\frac{1}{3} S_{\Delta}\right) \right] \mathbf{n}_{k,i',j';4,i,j} \cdot \mathbf{i} , \quad (16)$$

353 where the surface integral is taken over the triangle Ω_4 with the size of $S_{\Delta} = \frac{\sqrt{3}}{4} s_4^2$ and \mathbf{n} is the unit vector orthogonal
 354 to the boundary of the triangle Ω_4 (Fig. 5).

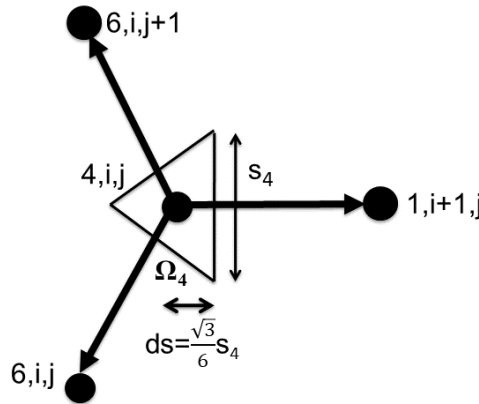
355 For the x -derivative $d_x h_4$ we obtain:

356
$$\partial_x h(\mathbf{r}_{4,i,j}) = \frac{\oint_{\Omega_4} fl(\mathbf{r}_{4,i,j}) \mathbf{n} \cdot d\mathbf{s}}{S_{\Delta}} = \frac{1}{3} \left[\partial_{\mathbf{n}_{1,i+1,j;4,i,j}} h(\mathbf{r}_{4,i,j}) - \frac{1}{2} \partial_{\mathbf{n}_{6,i,j;4,i,j}} h(\mathbf{r}_{4,i,j}) - \frac{1}{2} \partial_{\mathbf{n}_{6,i,j+1;4,i,j}} h(\mathbf{r}_{4,i,j}) \right]$$

357 , (17)

358 where the area of the triangle S_{Δ} , $\mathbf{n}_{1,i+1,j;4,i,j} \cdot \mathbf{i} = 1$, $\mathbf{n}_{6,i,j;4,i,j} \cdot \mathbf{i} = |\mathbf{n}_{6,i,j;4,i,j}| |\mathbf{i}| \cdot \cos 120^\circ = -\frac{1}{2}$ and
 359 $\mathbf{n}_{6,i,j+1;4,i,j} \cdot \mathbf{i} = |\mathbf{n}_{6,i,j+1;4,i,j}| |\mathbf{i}| \cdot \cos 210^\circ = -\frac{1}{2}$. The other corner points and y -derivatives are obtained by
 360 analogous formula.

361



362

363 **Fig. 5** Infinitesimal control volume: the computation of x - and y -derivatives from directional derivatives along cell
 364 edges.

365

366 We aim for a third-order approximation and therefore any third-order FDM scheme may be used. So far, we
 367 have defined FDM schemes for all collocation points being on the boundary of a hexagon. Using the points on the
 368 grid boundary, the flux around the surface of the hexagon into the grid is equal to the time derivative of the mass

369 inside the grid. The corner and edge amplitudes were obtained by above high-order FDM schemes for the hexagon.
 370 The approximation for the center amplitude will be then obtained by requiring mass balance. The center amplitude
 371 will be chosen in such a way that the time derivative of mass is consistent with the flux though the boundary. Mass
 372 conservation defines the implied amplitude uniquely.

373 We set the center point indexed $k = 0$ in the element (k, i, j) as an example. For any point x, y inside the
 374 hexagon with center $(0, i, j)$, we have the piecewise quadratic representation using the basis functions defined in
 375 Section 2. The sum given in the following formula represents the field limited to the chosen hexagon. Using the
 376 collocation basis defined in Eq. (6), the field representation for the chosen hexagon with center $(0, i, j)$ is :

$$377 \quad \partial_t h(\mathbf{r}) = \sum_{\Delta=1}^6 \partial_t h_0 \cdot e_{(0,i,j),\Delta}^c + \sum_{k=1}^9 \sum_{\Delta=1}^6 \partial_t h_k \cdot e_{(k,i,j),\Delta}^c + \sum_{k=6}^8 \sum_{\Delta=1}^6 \partial_t h_k \cdot e_{(k,i,j+1),\Delta}^c + \sum_{k=12}^{17} \sum_{\Delta=1}^6 \partial_t \bar{h}_k \cdot e_{(k,i,j),\Delta}^c, \quad (18)$$

378 where $\partial_t \bar{h}_k$ for $k = 12, 13, \dots, 17$ are diagnostically determined by the dynamic points $k = 0, 1, \dots, 9$ in the element
 379 (k, i, j) and $k = 6, 7, 8$ in the element $(k, i, j+1)$. Note that except $\partial_t h_0$ in Eq. (18), all other amplitudes $\partial_t h_i$ have
 380 already been computed. Therefore, it can easily be solved for $\partial_t h_0$. Let $m_k^0 = \sum_{\Delta=1}^6 \iint e_{(k,i,j),\Delta}^c(\mathbf{r}) dx dy$ be the mass
 381 of the collocation basis functions, as for the time derivative of mass $\partial_t M = \int \partial_t h \cdot dt$ of $\partial_t h$ inside the chosen
 382 hexagon we obtain:

$$383 \quad \partial_t M = \sum_{k=0}^9 \partial_t h_k m_{(k,i,j)}^0 + \sum_{k=6}^8 \partial_t h_k m_{(k,i,j+1)}^0 + \sum_{k=12}^{17} \partial_t \bar{h}_k m_{(k,i,j)}^0, \quad (19)$$

384 where the m_k^0 is the mass contained in the characteristic basis functions: $m_{(k,i,j)}^0 = \sum_{\Delta=1}^6 \iint e_{(k,i,j),\Delta}^c(\mathbf{r}) dx dy$ for $k =$
 385 $-6, \dots, 12$. $\partial_t M$ in Eq. (19) is known from the flux balance equation. Let $fl(\mathbf{r})$ be the flux of field h at the center
 386 point $k = 0$. Then, the surface integral of the flux is equal to $\partial_t M$:

$$387 \quad \oint_{\Omega_0} fl(\mathbf{r}) \mathbf{n}_0 \cdot d\mathbf{s} = \partial_t M, \quad (20)$$

388 where the surface integral is taken over the boundary Ω_0 which are the edges of the hexagon and \mathbf{n}_0 is the unit vector
 389 orthogonal to the hexagonal surface. Combining Eqs. (18)-(20), the only unknown $\partial_t h_0$ can therefore be solved.

390 The hexagonal example described above may be better understood by a 1-D example, which is given in the
 391 following:

392 Consider the 1-D homogeneous advection equation $\partial_t h = -\partial_x h$. The grid is $0, \frac{1}{2}, 1, \frac{3}{2}, 2, \dots$. The basis
 393 functions are defined in Eqs. (3)-(5). The grid is the interval (x_i, x_{i+1}) where $i = 0, 1, 2, 3, \dots$. The time derivative
 394 of the mass inside (x_i, x_{i+1}) is the flux difference.

395 Let the field $h(x)$ be defined by

396
$$h(x) = \sum_i h_i e_i(x) + A_i b_{i+\frac{1}{2}}^2(x) \quad (21)$$

397 with $e_i(x)$ being the piecewise linear function being 1 at point $x = x_i$ and being 0 at all other points (
 398 $x \in (x_{i-1}, x_{i+1})$), $b_{i+\frac{1}{2}}^2(x) = \frac{1}{2}(x^2 - \frac{ds^2}{4})$ where ds is the distance of a cell interval, A_i is the spectral amplitude
 399 belonging to the basis $b_i^2(x), i = \frac{1}{2}, \frac{3}{2}, \frac{5}{2}, \dots$. The integral of $b^2(x)$ is $-\frac{1}{12} ds^3$. The integral of the linear basis
 400 functions is $\frac{1}{2} ds$. The surface flux difference is $-(h_{i+1} - h_i)$ ($i = 0, 1, 2, \dots$). Then, Eq. (21) becomes:

401
$$-(h_{i+1} - h_i) = \frac{1}{2}(\partial_t h_{i+1} + \partial_t h_i) ds - \frac{\partial_t A_i}{12} ds^3 \quad (22)$$

402 As $b^2(0) = -\frac{1}{8} ds^2$ and $\partial_t h_{i+\frac{1}{2}} = \frac{1}{2}(\partial_t h_{i+1} + \partial_t h_i) + \partial_t A_i b^2(0)$, we have

403
$$\partial_t h_{i+\frac{1}{2}} = -\frac{3}{2ds}(h_{i+1} - h_i) - \frac{1}{4}(\partial_t h_{i+1} + \partial_t h_i) \quad (23)$$

404 In Eq. (23) $\partial_t h_i$ can be chosen arbitrarily and we use:

405
$$\partial_t h_i = \frac{a}{ds}(h_{i+\frac{1}{2}} - h_{i-\frac{1}{2}}) + \frac{b}{2ds}(h_{i+1} - h_{i-1}) \quad (24)$$

406 where coefficients a and b are defined in Steppeler et al. (2008).

407 Eqs. (23) and (24) are a 1-D version of the o2o3 scheme used with the hexagon. This is the scheme defined as
408 the o2o3 scheme in Ahlberg et al. (1967) without any tests.

409

410 **4. Advection experiments**

411 The aim of these advection experiments is to demonstrate that the sparse SEM describes the process properly.
412 This means that the accuracy expected from the third-order discretization scheme is achieved and that the results do
413 not indicate a serious shortcoming due to the sparseness. This should also be the case for marginal resolution. Second-
414 and third-order LGMs were proposed and used on squares in Steppeler (1976). In this study, the LGM operation has
415 further implemented on hexagons. We want to confirm that the methods presented here give results of about similar
416 quality.

417 Before the initialization of the advection test, we list the steps of the time loop for further explanation of
418 LGM.

419 ➤ Compute directional derivatives at corner and edge points ($k = 1, 2, \dots, 9$ in the element (k, i, j) and
420 $k = 6, 7, 8$ in the element $(k, i, j+1)$ in Fig. 1c)

421 ➤ Compute time derivatives at dynamic corner and edge points ($k = 1, 2, \dots, 9$ in the element (k, i, j)
422 and $k = 6, 7, 8$ in the element $(k, i, j+1)$ in Fig. 1c). At the corner points ($k = 1, 4, 6, 8$ in the element
423 (k, i, j) and $k = 6, 8$ in the element $(k, i, j+1)$ in Fig. 1c), average the three directional derivatives
424 of the lines meeting here

425 ➤ Perform ISE LGM at center points ($k = 0$ in the element (k, i, j) of Fig. 1c)

426 ➤ Perform fourth-order Runge-Kutta (RK4) time stepping in gridpoint space

427 No transformation of spectral coefficients to grid point space is necessary, as the grid point at the center ($k =$
428 0) is both spectral coefficient and spectral amplitude. Spectral coefficients which are different from gridpoint values

429 occur only at edge amplitudes ($k = 2, 3, 5, 7, 9$ in the element (k, i, j) and $k = 7$ in the element $(k, i, j+1)$ in Fig.
 430 1c).

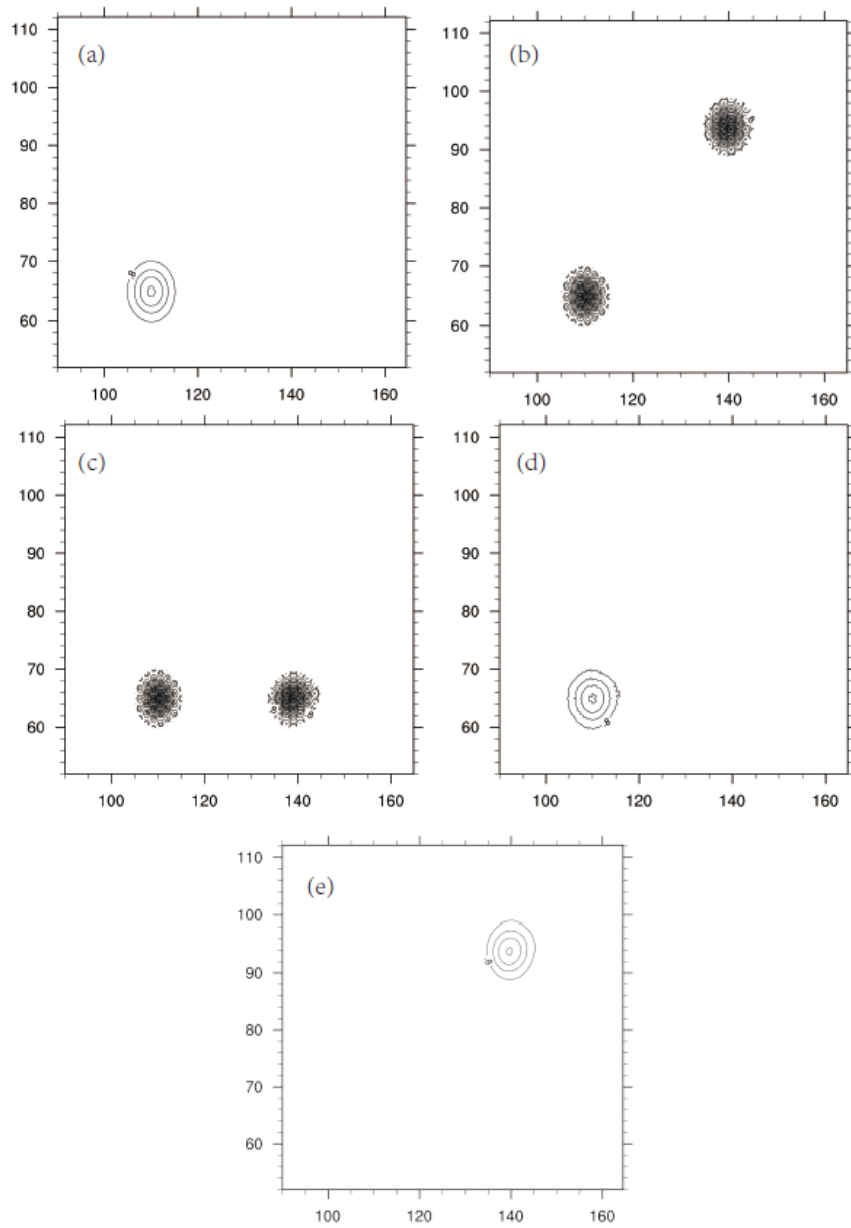
431 Now we perform the advection test. For the experiments done here, we assume the side length s of the
 432 hexagon to be $s = 2$. Fig. 6 gives the result of advection for a computational domain of $400 * 600$ grid point where
 433 $dx = 1$ and $dy = \frac{\sqrt{3}}{2}$ between every two points, and the timestep dt is 1.0 s with ninety timesteps. The components
 434 of advection velocity u and v are $(1, 1)$ for the first thirty timesteps, $(0, -1)$ for the second thirty timesteps and $(-1, 0)$
 435 for the last thirty timesteps. In order to obtain a solution where the initial field is reproduced after ninety timesteps,
 436 this velocity field is changed in time. In Fig. 6, thirty timesteps are done between plots and the plots are produced to
 437 show the sparse grid structure. The unused points are assigned a time derivative of zero. The initial values are shown
 438 in Fig. 6a and are given by:

$$439 \quad \rho_{i,j}^h = \rho_{i,j}^h(x_i^h, y_j^h) = \exp \left[- \left(\frac{x_i^h - x_0^h}{dx_{mid}} \right)^2 - \left(\frac{y_j^h - y_0^h}{dx_{mid}} \right)^2 \right], \quad (25)$$

440 where $\rho_{i,j}^h$ is the density of the tracer, (x_i^h, y_j^h) is the location of the density, $(x_0^h, y_0^h) = (110, 65)$ is the initial
 441 location of the density and dx_{mid} is the radii of the density. In Steppeler and Klemp (2017), it was determined by 1-
 442 D experiments that for $dx_{mid} = 8$ the second-order FDM scheme based on centered differences used there produced
 443 reasonable dispersion-free results, whereas heavy dispersion occurred for smaller values of dx_{mid} . Since the third-
 444 order approximation is used in this study, we may expect to obtain a reasonably dispersion-free results for $dx_{mid} = 4$
 445 .

446 Fig. 6a shows the initial values for $dx_{mid} = 4$. This is the same resolution as used in Steppeler and Klemp
 447 (2017). Of course, we may have better dispersion properties because using the third-order method. In Fig. 6a, Eq.
 448 (25) was used to compute all twenty-four points (twelve dynamic points and twelve unused points) for each (i, j) .
 449 Note that according to Fig. 1, the discretization group of points has twelve dynamic points and twelve diagnostic
 450 points which all are independent. These are more than the points belonging to a hexagon, as the discretization group
 451 is larger than one hexagon, as seen from Fig. 1. These plots are done using the NCAR Command Language (NCL)
 452 package. NCL is able to plot irregular distributions of amplitudes, as may occur with hexagonal grids. This way of

453 plotting is called unconventional plotting. When by advection the structure is moving away from its initial position,
454 unconventional plotting will make the hexagonal grid visible. Initial values at the unused points always remain visible.
455 When the structure has moved away from its initial position this means that the unused points have amplitude 0, at the
456 position of the structure and at the position of the initial field we see a negative picture of the solution, showing the
457 values according to Eq. (25) at the unused points.
458



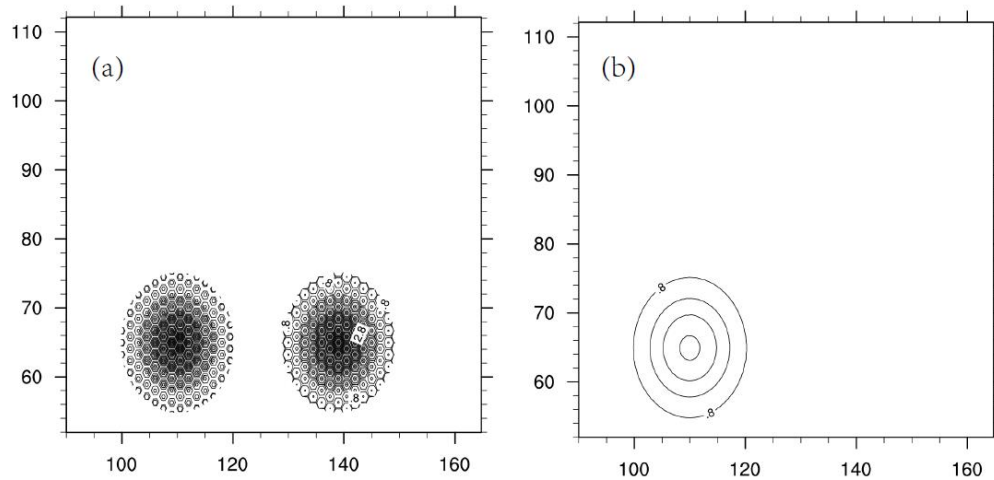
459

460 **Fig. 6** The advection results with time varying velocity field for $dx_{mid} = 4$. The initial value of the density field is
461 shown in (a). The advection results at thirty steps, sixty steps and ninety steps are shown in (b)-(d). In (b) and (c),
462 the values of the density field are the initial one at the left-hand side and the numerical result at the right-hand side.
463 The values of the field are set as 0 at the unused points where sparse grids are revealed. (e) is the results at thirty
464 steps except that the field for dynamically unused points is interpolated from the dynamic points. In this way, the
465 decrease of the maximum due to numerical dispersion can be seen. As expected for a third-order method, this
466 decrease is not to be noticed for a transport of 30 s.

467
468 We use the RK4 scheme for time stepping with $dt = 1$. Note that the RK4 time scheme with spatial centered
469 differences has a Courant-Friedrichs-Levy (CFL) stability condition of 2.8. Together with geometric considerations
470 given by Steppeler and Klemp (2017), the CFL condition for o2o3 will be 0.75×2.8 . The fourth-order spatial
471 differencing in comparison with lower order centered differences leads to a smaller CFL condition (see Durran 2010).
472 This leads to an estimate of the CFL number 1.4. Therefore, we may expect a stable solution using a timestep $dt = 1$.
473 We use thirty timesteps with $u = 1, v = 1$, thirty timesteps with $u = 0, v = -1$ and thirty timesteps with $u = -1, v = 0$.
474 After this the analytic solution is identical to the initial values. Experiments with varying timesteps confirmed this
475 estimate.

476 The result is shown in Figs. 6b–6e. The result shown in Fig. 6d have a slight difference from Fig. 6a by a
477 small numerical error. However, the plots given in Fig. 6b do not easily allow to see this, as the field is plotted on the
478 sparse grid. Fig. 6e is the same as Fig. 6b, but plotted on the full grid, where the points unused for dynamics are
479 interpolated. The unused points for Fig. 6d are not interpolated. They have the values they had in the beginning, as
480 the structure has reached the initial position again. The two parts of the field combine to give a smooth structure which
481 allows to see an eventual change of maximum due to a dispersion.

482



483

484 **Fig. 7** The advection results with time varying velocity field for a larger scale field ($dx_{mid} = 8$). **(a)** is the advection

485 results at sixty steps where the values of the density field are the initial one at the left-hand side and the numerical
 486 result at the right-hand side. The values of the field are set as 0 at the unused points where sparse grids are revealed.

487 **(b)** is the results at ninety steps except that the field for dynamically unused points is interpolated from the dynamic
 488 points. In **(d)** no interpolation is used, as the structure has been back to its initial place where the two parts of the
 489 field combine to give a smooth structure. **(e)** corresponds to **(b)** and contains the interpolation of the unused points.

490

491 Figs. 7 and 8 show the same advection tests with a different dx_{mid} for the initial density in Eq. (25) where

492 $dx_{mid} = 8$ and $dx_{mid} = 1$. Figs. 7a–7b show only the last two steps for a smooth solution. The error in reproducing

493 the initial field is reduced. Fig. 8 is the same for a small-scale field, which also reasonably reproduces the initial field.

494 The prediction of a very small-scale field is shown in Fig. 8. To indicate the small resolution, the hexagonal grid points

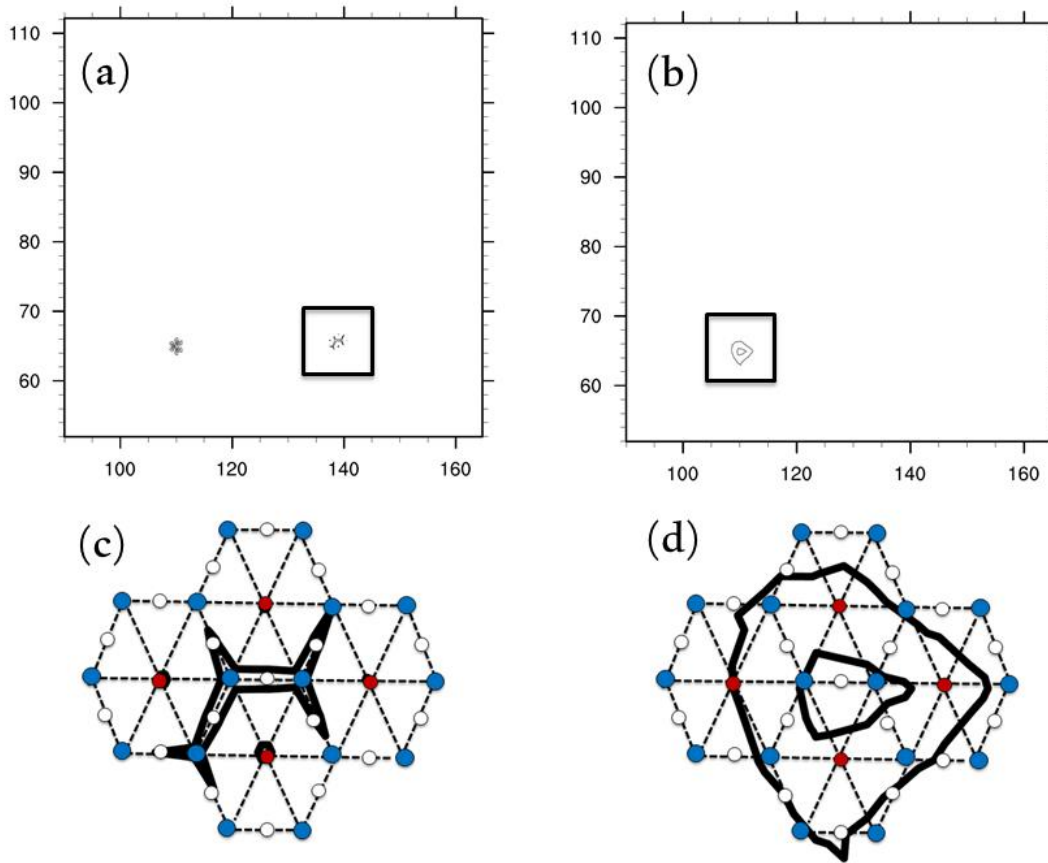
495 are shown in Fig. 8. It is clear that in each linear cross section there are very few points supporting the structure, but

496 the 2-D grid provides more points. In Appendix 1, we investigate the resolution of plane waves in the hexagonal grid

497 in comparison with a square grid. It is shown in Appendix 1 that plane waves in the hexagonal grid are better resolved

498 than in square grids.

499



500

501 **Fig. 8** As Fig. 7, for a small-scale field ($dx_{mid} = 1$), which represents a rather poor resolution. The red points in (c)
 502 and (d) carry amplitudes and possess small isolines which are covered by the red dots and a little black shadow is
 503 seen.

504

505 Then, we conducted another advection experiment where the components of advection velocity u and v are
 506 $(1, 0)$ and the initial density field is defined as follows:

507

$$\rho_{i,j}^h = \rho_{i,j}^h(x_i^h, y_j^h) = \left\{ \begin{array}{l} 4 \exp \left[-\left(\frac{x_i^h - 60}{dx_{mid}}\right)^2 - \left(\frac{y_j^h - 210}{dx_{mid}}\right)^2 \right], (x_0^h < 60, y_0^h < 210) \\ 4 \exp \left[-\left(\frac{x_i^h - 80}{dx_{mid}}\right)^2 - \left(\frac{y_j^h - 210}{dx_{mid}}\right)^2 \right], (x_0^h > 80, y_0^h < 210) \\ 4 \exp \left[-\left(\frac{x_i^h - 60}{dx_{mid}}\right)^2 - \left(\frac{y_j^h - 230}{dx_{mid}}\right)^2 \right], (x_0^h < 60, y_0^h > 230) \\ 4 \exp \left[-\left(\frac{x_i^h - 80}{dx_{mid}}\right)^2 - \left(\frac{y_j^h - 230}{dx_{mid}}\right)^2 \right], (x_0^h > 80, y_0^h > 230) \\ 4 \exp \left[-\left(\frac{x_i^h - 80}{dx_{mid}}\right)^2 \right], (x_0^h > 80, 210 < y_0^h < 230) \\ 4 \exp \left[-\left(\frac{x_i^h - 60}{dx_{mid}}\right)^2 \right], (x_0^h < 60, 210 < y_0^h < 230) \\ 4 \exp \left[-\left(\frac{y_j^h - 210}{dx_{mid}}\right)^2 \right], (60 < x_0^h < 80, y_0^h < 210) \\ 4 \exp \left[-\left(\frac{y_j^h - 230}{dx_{mid}}\right)^2 \right], (60 < x_0^h < 80, y_0^h > 230) \\ 4, (60 < x_0^h < 80, 210 < y_0^h < 230) \end{array} \right. , \quad (26)$$

508

which is used to test the sensitivity of the new LGM scheme. The density field is constructed to have sharper contours

509

and is nearly the characteristic function of a rectangle with slightly rounded contours. The timestep dt is 1.0 s with

510

210 timesteps while all other parameters share with the previous advection experiments. The advection in x -direction

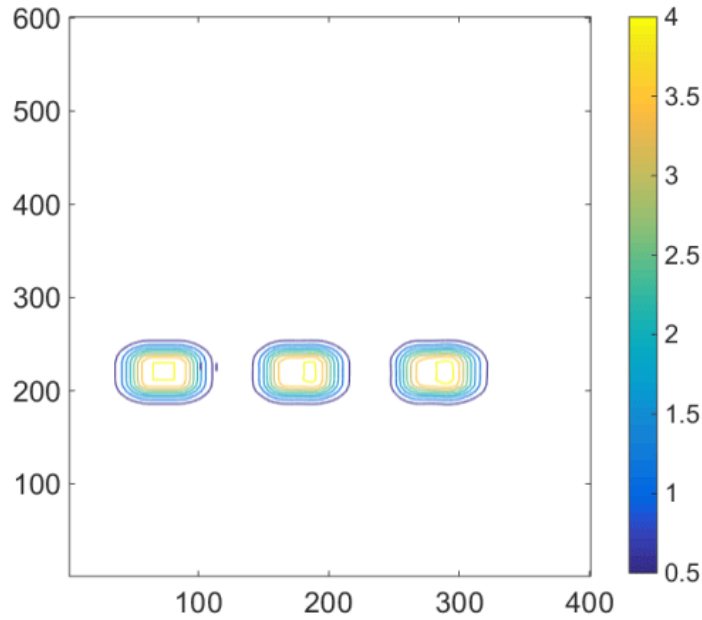
511

is shown in Fig. 9 which shows that the hexagonal grid is able to handle strong gradients. A standard way of plotting

512

is used, interpolating the unused amplitudes from the dynamic points.

513



514

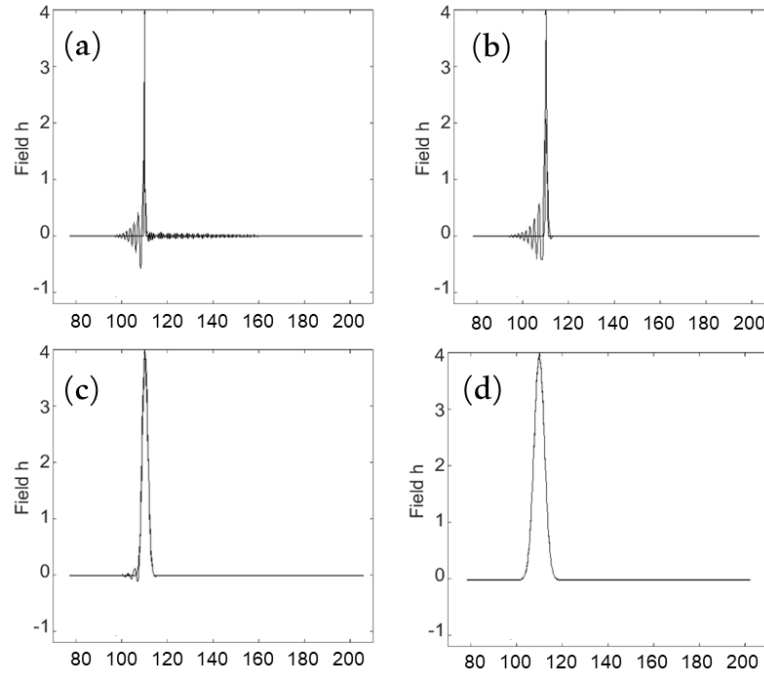
515 **Fig. 9** Advection of a field with strong gradients of a transport over $210 dx$ ($dx = 1$) by an integration of 210
 516 timesteps. The center of the initial tracer is located at $(70, 220)$ and the other two results show the tracers at $t = 105 s$
 517 and $t = 210 s$. The deformation of the field by dispersion is small. A standard way of plotting is used, interpolating
 518 the unused amplitudes from the dynamic points.

519

520 The scale of the structures used in the hexagonal grid was determined from 1-D experiments. The initial
 521 values were such that a small reduction of amplitude due to dispersion was presented. The same choice as in Steppeler
 522 and Klemp (2017) was used. We investigate this by using a 1-D version of a o2o3 scheme. For comparison, we plot
 523 the result of the second-order spectral element method (SEM2, Taylor et al 1997) which is known to converge in
 524 second order. A convergence test was done by computing the 1-D advection while systematically changing the
 525 resolution. The parameters are the same as the experiments in Fig. 6 except the resolution dx . The results are shown
 526 in Fig. 10. The resolution was changed systematically starting to 0.25 of the resolution used in Fig. 6 to four times this
 527 resolution. The errors, using the maximum norm, are given as Fig. 11. The convergence as seen in Fig. 11 is certainly
 528 third and appears to reach fourth order by super-convergence, which is observed also with SEM3 methods. From Fig.
 529 11, it can be seen that the high-order scheme at poor resolutions retains a rather high level of accuracy. The level of
 530 accuracy seen with the diagrams for the highest resolution is certainly more than needed in practice. For practical

531 purposes, it is less important how accurate a scheme is at very high resolutions, but rather, how soon a reasonable
532 accuracy is obtained.

533



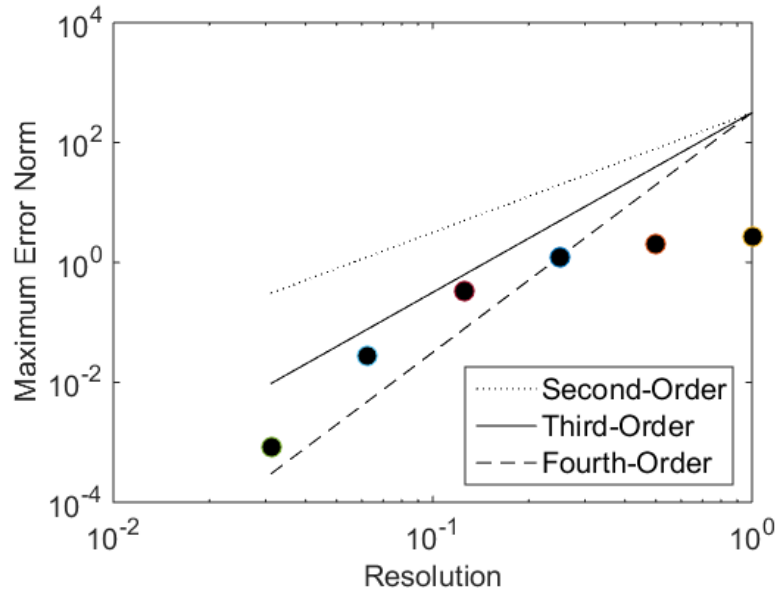
534

535 **Fig. 10** The advection over fixed 30 unit lengths for different resolutions. (a) $dx = 1.0$, (b) $dx = 0.5$, (c) $dx = 0.25$ and

536

(d) $dx = 0.125$.

537



538

539 **Fig. 11** Maximum error norms (dotted scatters) of third-order sparse SEM for different resolutions, starting from
 540 minimum resolution of $dx = 0.03125$ and doubling it by factors 2, 4, 8, 16, 32. The other three lines are the second-
 541 order (dotted), third-order (solid) and fourth-order (dashed) convergences for comparison.

542

543 5. Conclusions

544 Some simple experiments show that advection using sparse hexagonal grids is possible in third order with a
 545 piecewise quadratic polynomial representation. Using the o2o3 LGM, the 2-D sparse grid used only half the number
 546 of grid points as the full grid, meaning six points per cell against twelve points. The particular mapping of the cells
 547 and grid points to a structured i, j grid turned out to lead to a rather complicated computer program, which may be
 548 difficult to develop to further applications. Future developments will depend on defining a more convenient numbering
 549 of cells and grid points (see details in Appendix 1).

550

551 Acknowledgments

552 No authors reported any potential conflicts of interest. The paper was made possible by a number of research visits of
 553 the first author at NCAR, financed by NCAR. The city of Bad Orb supported this cooperation by providing office
 554 space. Dr. J. Li acknowledges the support of the National Natural Science Foundation of China (Grant No. 41905093),

555 the China Postdoctoral Science Foundation Funded Project (Grant No. 2016M601101) and China Scholarship Council
556 (No. 201904910136). Dr. F. Fang acknowledges the support of the Innovation of the Chinese Academy of Sciences
557 International Partnership Project (Grant No. Y56601M601) and the EPSRC grant: Managing Air for Green Inner
558 Cities (MAGIC) (EP/N010221/1).
559

560 **References**

- 561 Ahlberg JH, Nilson EN, Walsh JL (1967) The theory of splines and their application. Academic, New York.
- 562 Baumgardner JR, Frederickson PO (1985) Icosahedral discretization of the two-sphere. *SIAM J Numer Anal* 22:
563 1107–1115.
- 564 Cockburn B, Shu CW (2001) RungeKutta discontinuous Galerkin methods for convection-dominated problems. *J Sci*
565 *Comput* 16(3): 173–261.
- 566 Cote J, Beland M, Staniforth A (1983) A spectral element shallow water model on spherical geodesic grids. *Mon Wea*
567 *Rev* 111: 1189–1207.
- 568 Durran D (2010) *Numerical Methods fo Fluid Dynamics: with Applications to Geophysics*. Springer, New York.
- 569 Giraldo FX (2001) A spectral element shallow water model on spherical geodesic grids. *Int. J. Num Meth Fluids* 35:
570 869–901.
- 571 Kalnay E, Bayliss A, Storch J (1977) The 4th order GISS Model of the global atmosphere. *Beitrage zur Physik der*
572 *Atmosphäre* 50: 299–311.
- 573 Li J, Li J, Zheng J, Zhu J, Fang F, Pain CC, Steppeler J, Navon IM, Xiao H (2018) Performance of Adaptive
574 unstructured Mesh Modelling in idealized Advection cases over steep Terrains. *Atmosphäre* 9:444.
- 575 Marras S, Kelly JF, Moragues M, Müller A, Kopera MA, Vázquez M, Giraldo FX, Houzeaux G, Jorba O (2016) A
576 review of element-based Galerkin methods for numerical weather prediction: Finite elements, spectral
577 elements, and discontinuous Galerkin. *Arch Comput Method. E.* 23(4): 673-722.
- 578 Navon IM, Alperson Z (1978) Application of fourth-order finite differences to a baroclinic model of the atmosphere.
579 *Arch Met Geoph Biold, Ser A* 27: 1–19.
- 580 Peixoto PS, Barros SR (2013) Analysis of grid imprinting on geodesic spherical icosahedral grids. *J Comp Phys* 237:
581 61-78.
- 582 Rancic M, Purser RJ, Mesinger F (1996) A global shallow water model using an expanded spherical cube: Gnomonic
583 versus conformal coordinate. *Quart J Roy Meteor Soc* 122: 959–982.
- 584 Ringler TD, Heikes RH, Randall DA (2000) Modeling the atmospheric general circulation using a spherical geodesic
585 grid: A new class of dynamical cores. *Mon Wea Rev* 128: 2471–2485.
- 586 Sadourny R (1972) Conservative finite-difference approximations of the primitive equations on quasi-uniform
587 spherical grids. *Mon Wea Rev* 100: 136–144.

588 Satoh M, Masuno T, Tomita H, Miura H, Nasuno T, Iga S (2008) Nonhydrostatic icosahedral atmospheric model
589 (NICAM) for global cloud resolving simulations. *J Comput Phys* 227: 3486–3514.

590 Skamarock WC, Klemp JB (2008) A time-split nonhydrostatic atmospheric model for weather research and
591 forecasting applications. *J Comp Phys* 227 (7): 3465-3485.

592 Skamarock WC, Klemp JB, Duda MG, Fowler LD, Park SH (2012) A multiscale nonhydrostatic atmospheric model
593 using centroidal voronoi tessellations and C-Grid staggering. *Mon Wea Rev* 140: 3090-3105.

594 Staniforth A, Thuburn J (2012) Horizontal grids for global weather and climate prediction models: a review. *Quart J*
595 *Roy Meteor Soc* 138(662): 1-26.

596 Steppeler J (1987) Galerkin and finite element methods in numerical weather prediction. Duemmler, Bonn.

597 Steppeler J (1976) The Application of the Second and Third Degree Methods. *J Comp Phys* 22: 295–318.

598 Steppeler J (1979) Difference Schemes with Uniform Second and Third Order Accuracy and Reduced Smoothing. *J*
599 *Comp Phys* 31: 428-449.

600 Steppeler J, Klemp JB (2017) Advection on cut-cell grids for an idealized mountain of constant slope. *Mon Wea Rev*
601 145: 1765–1777.

602 Steppeler J, Li J, Fang F, Zhu J, Ullrich PA (2019) o3o3: a variant of spectral elements with a regular collocation grid.
603 *Mon Wea Rev* 147(6): 2067-2082, doi: 10.1175/MWR-D-18-0288.1.

604 Steppeler J, Prohl P (1996) Application of finite volume methods to atmospheric models. *Beitr Phys Atmos* 69: 297–
605 306.

606 Steppeler J, Ripodas P, Thomas S (2008) Third order finite difference schemes on isocahedral-type grids on the sphere.
607 *Mon Wea Rev* 136: 2683–2698.

608 Taylor M, Tribbia J, Iskandarani M (1997) The spectral element method for the shallow water equations on the sphere.
609 *J Comp Phys* 130: 92–108.

610 Tomita H, Tsugawa M, Satoh M, Goto K (2001) Shallow water model on a modified isosahedral geodesic grid by
611 using spring dynamics. *J Comp Phys* 174: 579–613.

612 Weller H, Thuburn J, Cotter CJ (2012) Computational modes and grid imprinting on five quasi-uniform spherical C
613 grids. *Mon Wea Rev* 140(8): 2734-2755.

614 Williamson DL (1968) Integrations of the barotropic vorticity equation on a spherical geodesic grid. *Tellus* 20: 643–
615 653.

616 Williamson DL (2007) The evolution of dynamical cores for global atmospheric models. J Meteorol Soc Jpn Ser II
617 85: 241-269.

618 Zängl G, Reinert D, Rípodas P, Baldauf M (2015) The ICON (ICOsahedral Non-hydrostatic) modelling framework
619 of DWD and MPI - M: Description of the non - hydrostatic dynamical core. Quart J Roy Meteor Soc
620 141(687): 563-579.

621

622

643
$$\mathbf{r}_{i,k} = \mathbf{r}_{i,0} + \left(s \cdot \cos\left(\pi + (k-1)\frac{\pi}{3}\right), s \cdot \sin\left(\pi + (k-1)\frac{\pi}{3}\right) \right) \quad (\text{A1})$$

644 The edge nodes $k = 2, 4, 6, 8, 12$ are obtained by

645
$$\mathbf{r}_{i,k} = \mathbf{r}_{i,k-1} + \frac{\sqrt{3}}{2} \left(s \cdot \cos\frac{\pi}{3}, s \cdot \sin\frac{\pi}{3} \right) \quad (\text{A2})$$

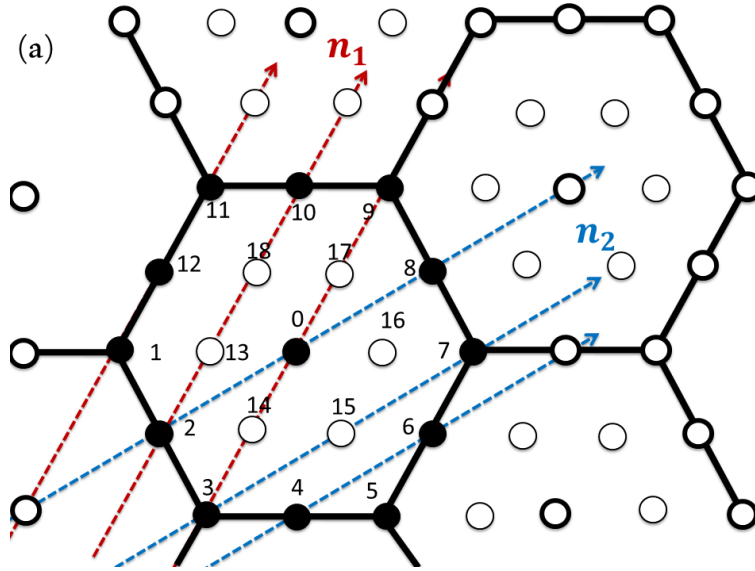
646 For the diagnostic inner points $k = 13$ to 18 , we have

647
$$\begin{aligned} \mathbf{r}_{i,k} &= \mathbf{r}_{i,0} + \frac{1}{2} \left(s \cdot \cos\left(\pi + (2k - 25 - 1)\frac{\pi}{6}\right), s \cdot \sin\left(\pi + (2k - 25 - 1)\frac{\pi}{6}\right) \right) \\ &= \mathbf{r}_{i,0} - \frac{1}{2} \left(s \cdot \cos\left(\frac{k-1}{3}\pi\right), s \cdot \sin\left(\frac{k-1}{3}\pi\right) \right) \end{aligned} \quad (\text{A3})$$

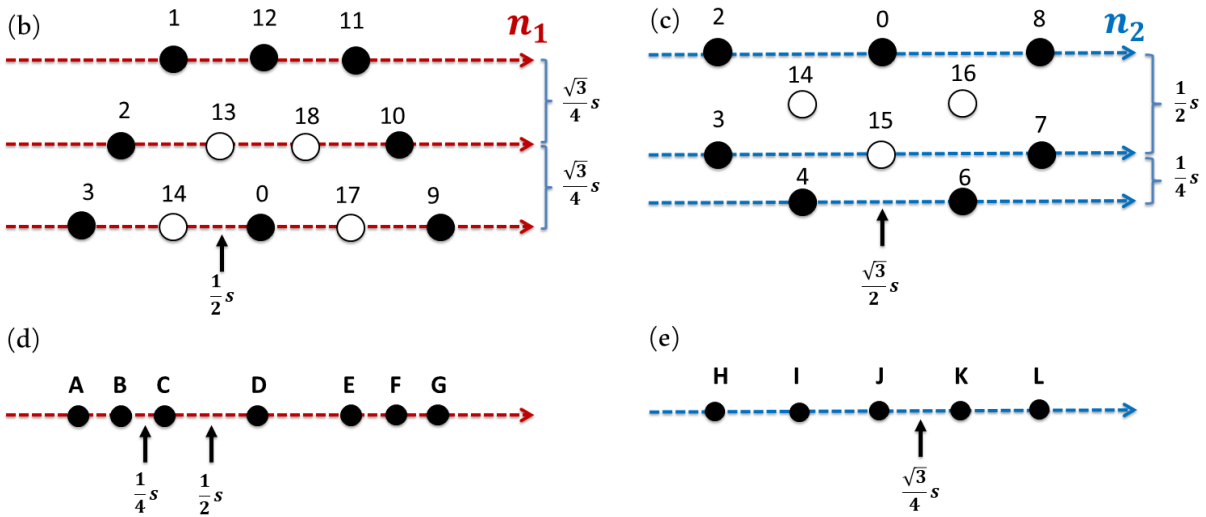
648 The full grid consists for each i of all points $k = 0$ to 18 . The points numbering $13, 14, 15, 16, 17, 18$ are
649 unused in the sparse grid. The sparse grid collocation therefore consists of the points i, k ($k = 0$ to 12) which are the
650 mid-point $k = 0$ and points on the boundary. The sparse grid is redundant, as all points with $k > 0$ belong to more than
651 one hexagon. For example in Fig. A1, the point $9_{i',j'}$, is also point $1_{i'+1,j'+1}$ and $5_{i',j'+1}$. The point $10_{i',j'}$ belongs only to
652 one other hexagon: $i', j'+1$. These redundant points of the collocation grid can be used to represent discontinuous
653 functions.

654 The index is defined with respect to the orthogonal basis \mathbf{i}_s and \mathbf{j}_s shown in Fig. A1. This method of
655 indexing is suitable for model areas being approximately square. A rhomboidal area can be achieved by changing the
656 definition of the basis \mathbf{i}_s and \mathbf{j}_s shown in Fig. A1.

657 It was shown by Steppeler (1979) that the anisotropy of the square grid can lead to the deformation of
658 structures, such as the destruction of the symmetry of a circular wave. It may be useful to show the connection to 1-D
659 discretizations. In Fig. A2, two vectors \mathbf{n}_1 and \mathbf{n}_2 are given and for each of these directions grid lines are shown in
660 Fig. A2 (b) and (c) which meet hexagonal grid points and thus determine a 1-D grid. Fig. A2 shows the lines and the
661 1-D grids created by them. \mathbf{n}_1 and \mathbf{n}_2 form a 30° angle. The situation is similar as with square grids, where two 1-
662 D grids are generated by lines forming a 45° angle. For square grids, the implied grids have grid lengths of dx in x
663 direction and for the 45° line the grid length $dx' = \frac{dx}{\sqrt{2}}$. For the square the grids seen by a plane wave in the direction
664 of either x or the diagonal are all the same, as each line determines the same grid.



665



666

667 **Fig. A2** Two examples of lines resulting in 1-D grids for two directions. The combined grid which is seen by a plane

668 wave in the directions of the arrows $\mathbf{n}_1 = (\cos 60^\circ, \sin 60^\circ) = \left(\frac{1}{2}, \frac{\sqrt{3}}{2}\right)$ and $\mathbf{n}_2 = (\cos 30^\circ, \sin 30^\circ) = \left(\frac{\sqrt{3}}{2}, \frac{1}{2}\right)$ is

669 shown in (d) and (e).

670

671 For 1-D grids in the direction of \mathbf{n}_1 generated by hexagonal grids, three types of irregular grid appear, shown

672 in Fig. A2 (b). A plane wave in the directions \mathbf{n}_1 or \mathbf{n}_2 sees one of the two grids (Fig. A2 (d) and (e)). They have

673 the average resolution dx' ($\frac{3}{8}s$ for Fig. A2 (d) and $\frac{\sqrt{3}}{4}s$ for Fig. A2 (e)). This is of higher resolution than each of the

674 original grids shown in Fig. A2 (b) or (c). It has also a higher resolution than the underlying regular square grid of
675 resolution $\frac{1}{2} s$. For the gradients of the fluxes at corner points in \mathbf{n}_1 or \mathbf{n}_2 direction, the o2o3 scheme proposed in
676 this paper uses one-sided derivatives and averages them over the three directions shown in Fig. 5. For a structure being
677 smooth in the direction vertical to \mathbf{n}_1 or \mathbf{n}_2 , the derivative at one point uses points forming a different grid for each
678 of the lines indicated in Fig. A2. Thus, the resolution of a plane wave is that of the 1-D grids shown in Fig. A2 (d) and
679 (e). The irregularity of the plane wave grids is of a small scale which means that while some points are near to each
680 other, they have large differences in grid length. The pattern of small and larger grid lengths repeats itself. These grids
681 have a higher resolution than the plane wave grids for the square.

682 It was shown by Steppeler and Klemp (2017) for the example of centered differences that such small-scale
683 irregularity gives a quality of simulation corresponding to the average grid length. It can be seen that the average grid
684 for plane waves is smaller than the grid used on the hexagonal sides. The values of the average grids given above
685 should be compared to those corresponding to the square grid. For the square grid, we obtain $\frac{s}{2}$ and $\frac{s}{2\sqrt{2}}$ for the
686 averaged resolutions in two directions. The relation of the two grids is 1.17 for the hexagon and 1.47 for the square.
687 These numbers are a measure of the isotropy of the grid, which is higher for hexagons. The maximum plane wave grid
688 length is also smaller for the hexagon ($0.433 s$) than for the square ($0.5 s$). The maximum of the two grids for different
689 directions of plane waves is the resolution of the scheme. A small resolution in just one direction is not useful except
690 for the case that the nature of the solution requires a deformed grid.

691 The indices of the inherent 1-D grids and their computation from the hexagonal indices can be seen from Fig.
692 A2 (b) and (d) or (c) and (e). The hexagonal version of the grid for the method o3o3 (Steppeler et al. 2019) is obtained
693 from the o2o3 hexagonal grid by having four instead three points on each edge and the center point no longer carries
694 an amplitude.